

Chapter 13. Wind Speed and Direction

Frank M. Monaldo

Johns Hopkins University Applied Physics Laboratory, Laurel, Maryland USA

Robert Beal

Johns Hopkins University Applied Physics Laboratory, Laurel, Maryland USA

13.1 Introduction

Global wind vector measurements from space aid meteorologists in weather forecasting and contribute to the understanding of atmospheric dynamics, air-sea interaction, and climatology. Radar measurements by scatterometers and synthetic aperture radars (SARs) have been used to measure wind vectors from space. In this chapter, we provide a historical context to the active microwave wind vector measurements from space and describe the latest efforts to routinely measure high-resolution wind fields with SAR. We also provide examples of some meteorological phenomena uniquely visible in SAR imagery. Finally, we discuss the future of SAR wind imagery and the blending of wind speeds derived by SAR and scatterometer.

At very low wind speeds and at microwave frequencies, the ocean surface is smooth, almost glass-like. Under these conditions, the radiation from a side-looking radar will reflect away from the radar and yield little or no backscattered power. As the wind speed increases, the surface roughens and backscattered power increases. The backscattered power is greatest when the radar look direction and the wind direction are aligned. However, there is a slight asymmetry. The backscattered power for winds blowing directly toward the radar is greater than the power for winds blowing directly away from the radar. The changes in backscattered power as a function of wind speed and direction form the basis of the remote sensing of wind speed and direction from spaceborne radar.

At a given wind speed and direction and radar geometry, the normalized radar cross section (NRCS) can be empirically predicted. Unfortunately, the inverse is not true—a given NRCS does not correspond to a unique wind speed and direction pair. Figure 13.1 is a three-dimensional plot of a microwave wind speed model function for a 25° radar incident angle. The x -axis represents wind speed, the y -axis represents the angle between the radar look direction and the local wind direction, and the z -axis represents the radar cross section. A single radar cross section would define a plane parallel to the xy -plane. This plane intersects the model function at a large number of wind speed and direction pairs. Thus, many different wind speed and direction pairs could produce a particular radar cross section.

Measuring the surface NRCS from a number of different aspect and incident angles reduces the number of potential solutions and alleviates this inversion difficulty. This multi-measurement approach to inversion is the basis of conventional spaceborne radar scatterometer measurements of the wind vector.

13.2 Backscattering

In 1913, Sir William Bragg demonstrated that when radiation scatters from a crystal, there is increased backscatter when the radiation wavelength corresponds to the crystal lattice spacing. The periodic structure of the lattice produces constructive interference and increases reflected power. By extension, *Wright* [1960] showed that the ocean NRCS for incident angles

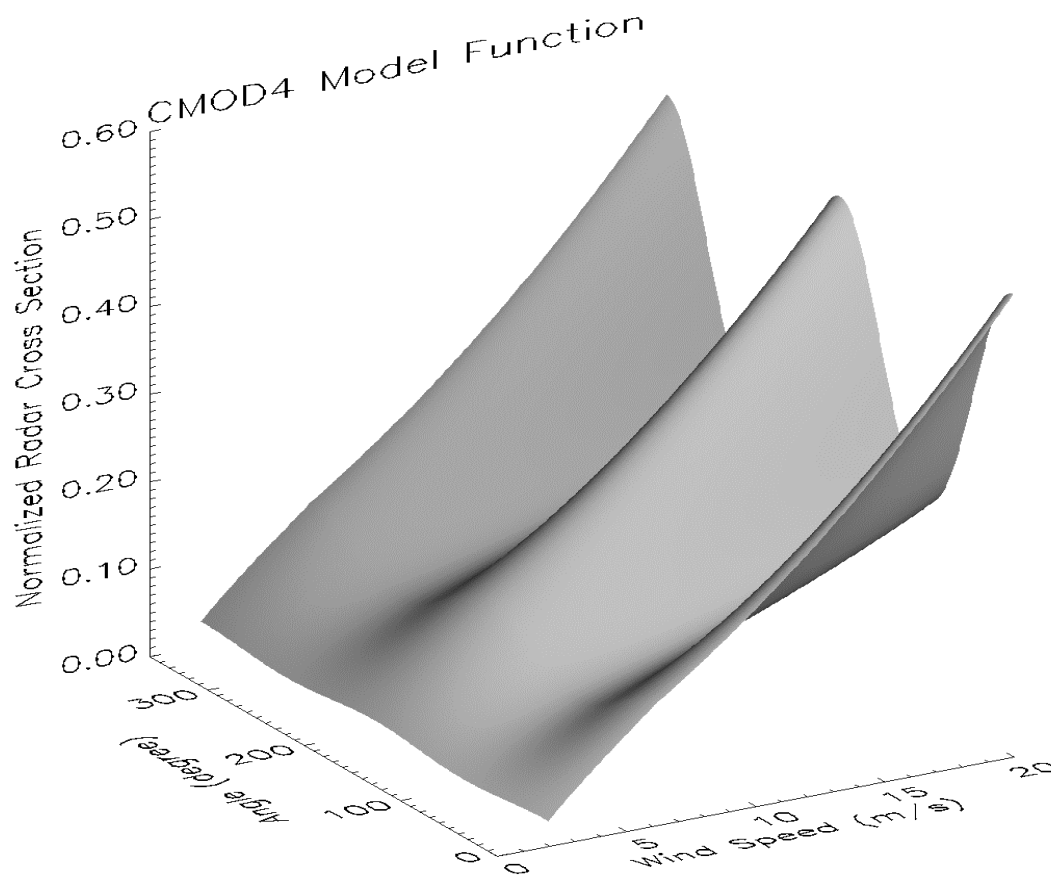


Figure 13.1. The CMOD4 geophysical model function relating wind speed and direction with respect to the radar to normalized radar cross section. For this case, the radar nadir incident angle is 25°.

between 20° and 60° primarily depends on the waves on the surface that match the radar wavelength projected onto the surface, in which case the ocean waves are called Bragg waves. Despite this work and more modern theoretical developments, scatterometry relies largely on empirical geophysical model functions relating wind speed and direction to NRCS rather than theoretical estimates of this relationship [Wentz *et al.*, 1984; Stofflen and Anderson, 1997; Romeiser *et al.*, 1997; Brown, 2001]. It is important to remember that waves of short wavelength are the first to be generated by the wind and the fastest to decay when wind speed decreases. As a consequence, the higher the frequency of the radar, the more quickly changes in wind speed are reflected in changes in surface roughness and backscattered radar power. The radar frequency and, hence, the surface wavelength of interaction are critical parameters in the design of a microwave scatterometer.

13.3 Scatterometers

An experimental wind speed vector scatterometer flew aboard Skylab [Moore *et al.*, 1974]. Based on this experience, a more sophisticated scatterometer flew aboard the SEASAT satellite in 1978. SEASAT's scatterometer used multiple stick-antenna and operated at 14.6 GHz (wavelength 2.1 cm). The instrument generally yielded four possible wind speed and direction pairs at a 50-km spatial resolution over two symmetric 500-km-wide swaths [Boggs, 1982]. The best estimate for the appropriate wind speed and direction pair was selected by

Wind Speed and Direction

comparing possible solutions with numerical weather model wind vector predictions and considerations of continuity. Typically, SEASAT achieved an accuracy of 1.6 m s^{-1} with respect to buoy measurements [Brown, 1983; Hawkins and Black, 1983; Pierson, 1983; Wentz et al., 1986].

Since then, scatterometers have flown aboard ERS-1 (1991), ERS-2 (1995), ADEOS-1 (1996) and QuikSCAT (1999) spacecraft. The latest SeaWinds [Spencer et al., 2000] scatterometer on QuikSCAT represents a significant departure from previous scatterometer designs. SeaWinds uses two rotating pencil beam radars to measure NRCS at different aspect angles and incident angles at 25-km resolution over an 1800-km-wide swath. Multi-stick scatterometers have more uniform performance across their entire swaths than rotating beam scatterometers, but do not make measurements nadir to the spacecraft. The performance of a rotating pencil beam scatterometer depends on the geometry of the beams as they measure the NRCS of the surface. There are two looks at each point from each of the two beams at different incident angles. At the outer edge of the swath, there are only two looks from the large incident angle beam. Also, near the nadir ground track, the fore and aft looks provide less direction information. Scatterometers have become the instrument of choice for global wind vector measurements. The recent decision to use a rotating beam scatterometer as opposed to the stick variety is a practical one based on ease and cost of implementation.

13.4 Synthetic Aperture Radar (SAR)

SEASAT was also equipped with an L-band (20-cm wavelength) SAR that created high (25 m) resolution, 100-km-wide radar images. These images have a resolution three orders of magnitude finer than can be achieved by conventional spaceborne scatterometers and were primarily expected to measure ocean surface wave spectra and not winds. While conventional scatterometry is useful and important for wind vector measurement on a global scale, it fails close to shore. Contamination from land reflections degrades scatterometer measurements near land. By contrast, high-resolution SAR imagery offers the prospect of extending wind speed measurements right up to the shore to obtain information valuable to coastal areas.

Despite the fact that a SAR views the surface at only one aspect angle, clear wind speed signatures were visible in even the earliest SEASAT SAR images in which there were bright areas associated with high wind speed. In the early imagery, there were other areas where the wind speed was so low that the ocean surface was smooth and, therefore, reflected radar energy and resulted in dark patches in SAR images.

Early comparisons by Jones et al. [1981] and Weissman et al. [1979] demonstrated a correlation between the L-band SEASAT SAR image intensity and SEASAT scatterometer wind speed. The SEASAT SAR, however, was not sufficiently well calibrated to be easily used with NRCS geophysical model functions to estimate wind speed. Even after empirical adjustment, the lack of wind direction information hindered the application of NRCS measurements for the unique and quantitative retrieval of wind speed.

Early investigations of SAR imagery and scatterometer data indicated that both instruments were affected by the details of air-sea interaction in the planetary boundary layer [Brown, 1986]. In a seminal paper, Gerling [1986] observed linear features aligned with the direction of the wind on the scale of a few kilometers in SEASAT imagery. Gerling postulated that wind rows [Brown, 1980; Fu and Holt, 1982] were responsible for these linear structures. An area of downward flow causes more surface roughness and therefore higher backscatter than an area of upward flow, thus creating a periodic structure in a SAR image. Using Fourier

transform techniques, *Gerling* further showed that he could estimate wind directions, albeit with a 180° ambiguity, from these wind row signatures.

When present, wind rows can indicate the general direction of the prevailing wind depending on the thermal stratification of the planetary boundary layer [*Brown and Lee, 1972*]. The angular difference between linear features in a SAR image and the wind direction depends on atmospheric stability [*Brown, 1980*]. If the atmosphere is very stable near the surface (a positive air-sea temperature difference) wind rows may disappear entirely. In addition, at times there are ocean circulation features at the same spatial scales that may be confused with wind rows.

The 20-cm radar wavelength of the SEASAT SAR implies that the NRCS depends on surface waves of about the same wavelength. When the wind blows, it takes time for waves of this wavelength to be generated. Higher radar frequencies are responsive to shorter ocean waves. These shorter ocean waves, in turn, are more immediately responsive to changes in wind speed. Wind speeds generally had to be above 2 m s⁻¹ before the SEASAT SAR imagery yielded an appreciable radar return. The SEASAT SAR did not have an optimum frequency for wind speed measurement. The Ku-band (2.1 cm wavelength) SEASAT scatterometer, by contrast, was more responsive to wind speed variations.

In 1991, the European Space Agency launched the ERS-1 satellite. ERS-1 was equipped with a combined C-band (5-cm wavelength) vertical-vertical (VV) polarization SAR/scatterometer Active Microwave Instrument (AMI). The use of this new frequency necessitated the development of a C-band geophysical model function relating wind speed and direction to NRCS. The result of these efforts was the development of the CMOD4 function [*Stofflen and Anderson, 1997; IFREMER, 1996*]. Although there are certain small variations of this model function found in the scientific literature, the C-band VV-polarization response to wind speed and direction is well characterized.

Vachon and Dobson [1996], *Wackerman et al. [1996]* and *Fetterer et al. [1998]* used the fruits of these efforts to extend the work of *Gerling* to estimate wind speed and direction from the ERS-1 SAR. In 1995, the Canadian RADARSAT-1 satellite was launched from Vandenberg Air Force Base in California. The primary purpose of its C-band horizontal-horizontal (HH)-polarization SAR is the monitoring of sea ice conditions. In its wide-swath mode, the SAR imagery covers a 500-km swath at 100-m resolution.

While the timeliness of SAR imagery is important in sea ice monitoring, the time scales of changes for ice are longer than the six- to twelve-hour time scales of weather fronts. Until recently, sea ice monitoring was virtually the only operational use of SAR imagery. SAR data processing requirements and the sheer data volume have proved in the past to be an important limitation in using SAR imagery for making high-resolution wind speed measurements in an operationally useful context. Once the signal data are received, they must be merged with satellite ephemeris data and processed into calibrated NRCS imagery. The imagery must then be converted into wind speed estimates. Fortunately, rapid improvements in data processing have alleviated this challenge. Presently, “quick-look” RADARSAT-1 SAR imagery can be produced in one to two hours depending on the processing center.

In 1998, the National Oceanic and Atmospheric Administration (NOAA), in conjunction with Johns Hopkins University Applied Physics Laboratory (JHU/APL) and Veridian Systems Division, established a quasi-operational system for estimating wind fields from the RADARSAT-1 SAR. The program began as the Storm Watch Project and has evolved into the Alaska SAR Demonstration Project [*Pichel and Clemente-Colón, 2000*].

In this project, RADARSAT-1 SAR data are downloaded in real-time when the satellite

Wind Speed and Direction

is in view of the Alaska Satellite Facility (ASF) ground station. ASF quick-look processes the data into calibrated SAR imagery. Next, the data are electronically forwarded to NOAA in Camp Springs, Maryland where they are converted into wind speed estimates, and the results are subsequently posted on the World Wide Web. During the first two years of operation, the total time from satellite to web was about 5 to 6 hours. Recently, with substantial improvements in computer speed, this time has been reduced to 3 hours. For best use in an operational weather forecasting context, the total time needs to be reduced to approximately two hours. The limiting time factor now seems to be the SAR image processing. This limitation will gradually diminish with increased computer speed.

There were several challenges associated with using RADARSAT-1 SAR imagery for determining real-time wind speeds. The first challenge involved choosing the appropriate wind speed model function. The CMOD4 model function, while appropriate in frequency, was developed for VV polarization. The RADARSAT-1 SAR operates at HH polarization. *Thompson et al.* [1998] addressed this deficiency by proposing an incident-angle dependent polarization ratio function that relates the VV-polarization NRCS to HH polarization NRCS.

The second challenge involves choosing which wind direction to use in SAR wind speed retrieval. One approach is to use linear features in the SAR image, such as *Gerling* [1986], *Vachon and Dobson* [1996], *Wackerman et al.* [1996], *Fetterer et al.* [1997], and *Horstmann et al.* [2001] have done, to estimate wind direction. Though often successful, there are times when the wind row signature is weak or when there are features associated with other phenomena on the same spatial scale. An alternative approach is to use wind directions from model predictions. Model-produced directions have the advantage of always being available. However, their spatial resolutions are generally far worse than the SAR resolution. For the Alaska SAR Demonstration, both approaches were taken in parallel.

Veridian Systems Division implemented software that divides wide-swath SAR images into smaller 25 km \times 25 km sub-images. For each of those smaller images, Fourier transform techniques are used to estimate wind direction, albeit with a 180° directional ambiguity. This direction is combined with the mean cross section of the smaller image to estimate wind speed.

In parallel, JHU/APL software uses wind direction predictions provided on a 1° \times 1° longitude-latitude grid by the U.S. Navy's Navy Operational Global Atmospheric Prediction System (NOGAPS) model. These directions are interpolated down to each pixel in a RADARSAT-1 SAR image and used with the radar cross section measurement to infer wind speed.

Figure 13.2 is a normalized radar cross section image from the RADARSAT-1 SAR acquired on 19 March 2001 at 0248 UTC off the western coast of Canada. Note the systematic falloff in NRCS from near to far range (left to right) in the image. This falloff is created because NRCS decreases with incident angle. Figure 3 is the same image after it has been converted to wind speed and color-coded. Wind speed structures in the far range are now apparent after appropriate correction for the falloff in response with incident angle.

In Figure 13.3, the land areas are shown in gray as topographic maps. The large arrows represent the wind speed and direction from the NOGAPS model. The smaller arrows represent the wind speeds from the Veridian Systems Division processing. There is general agreement between the SAR wind speeds and model predictions. It is also clear that the imagery reveals many important coastal wind features. Note the high wind funneling through the inner passage from Juneau southward. This image reveals a phenomenon commonly seen in SAR wind speed images, namely gap flow. Gap flow occurs as the wind passes over topographic features and is channeled into intensified flow. This image also illustrates the high spatial variability of the



Figure 13.2. RADARSAT-1 (C-band, HH) SAR normalized radar cross section image acquired on 19 March 2001 0248 UTC as processed by the Alaska Satellite Facility. Although the signatures in the NRCS representation are faint, the increased backscatter caused by gap flows is visible. ©CSA 2001.

wind in coastal areas. While wind speeds may be unchanging in the direction of flow, orthogonal to the wind direction, wind speeds can vary by over 10 m s^{-1} over a few kilometers.

In Alaska, local stories abound about the sudden appearance of *williwaws*—storm-force winds that have been known to overwhelm ships. Figures 13.4 and 13.5 help explain such observations. Figure 13.4 is a RADARSAT-1 SAR NRCS image, acquired 31 October 2000 at 0344 UTC. Figure 13.5 is the corresponding wind field image. It shows intensified gap flow between Kodiak Island and the Kenai Peninsula.

Wind Speed and Direction

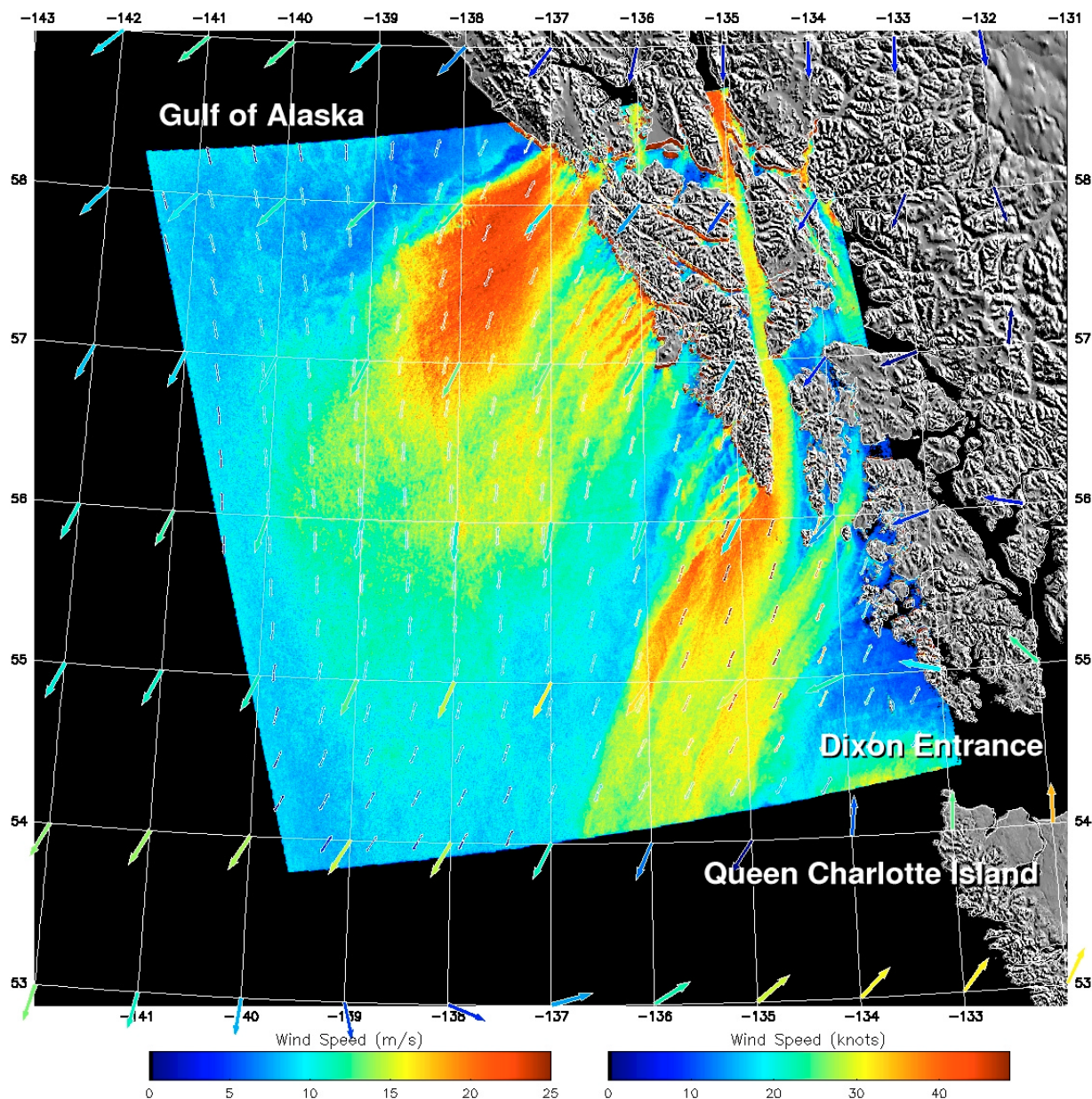


Figure 13.3. RADARSAT-1 SAR wind speed image produced for the Alaska SAR Demonstration Project. The colors represent wind speed up to a maximum of 25 m s^{-1} . The large color-coded arrows represent the model winds used for the SAR wind retrieval. The small arrows represent wind vectors from the Veridian System Division retrieval process. The imagery was acquired on 19 March 2001 at 0248 UTC.

The sub-kilometer resolution of SAR wind speed imagery has permitted the observation of atmospheric phenomena that has been difficult with other instruments. The NRCS and wind speed images in Figures 13.6 and 13.7 were acquired on 4 May 2001 at 0526 UTC at the western end of the Aleutian Island chain. Of particular interest in these images are the roll vortices being shed off Gareloi Island. The vortices have a periodicity of about 10 km and extend for over 200 km.

Figures 13.8 and 13.9 represent additional meteorological phenomena observable in SAR imagery. The SAR-derived wind speed image in Figure 13.8 covers the northern portion of the



Figure 13.4. RADARSAT-1 (C-band, HH) SAR NRCS image near Kodiak Island, Alaska. The bright or high cross section areas represent high wind speeds. This image was acquired on 31 October 2000 0344 UTC and was processed by the Alaska Satellite Facility. ©CSA 2000.

Gulf of Alaska. As wind blows north from the Gulf of Alaska, it runs into high topography along the coast forming a high-speed barrier jet [Overland, 1984]. The image in Figure 13.9 covers part of the Alaska Peninsula and the Aleutian Islands. In the image, there is a uniform wind from the northwest. As the wind flows over the topography, atmospheric internal waves are generated. This wind speed image demonstrates the characteristic periodic structure of atmospheric internal waves.

Wind Speed and Direction

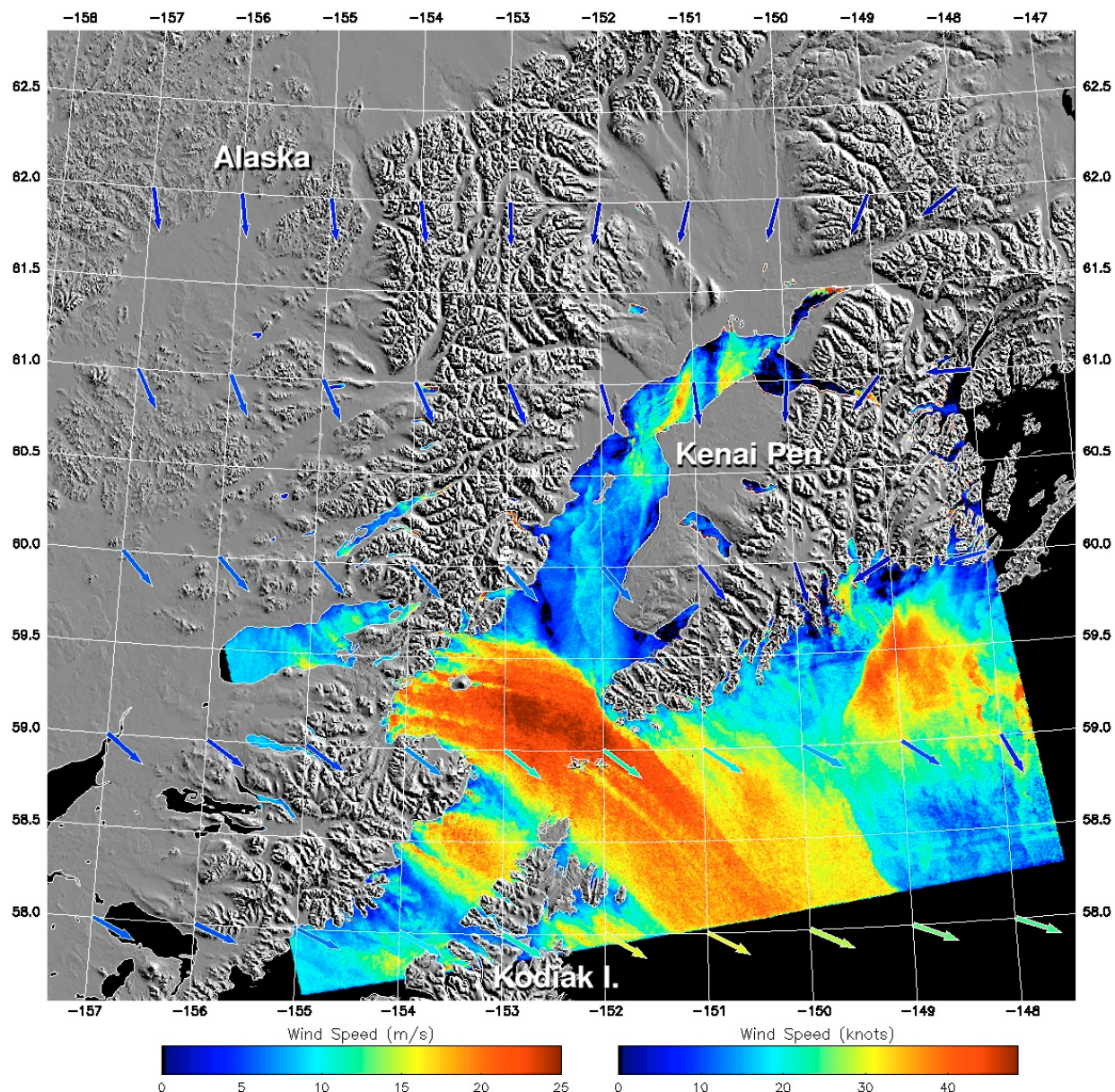


Figure 13.5. RADARSAT-1 SAR wind speed image near Kodiak Island, Alaska. The intensified gaps flows, reaching over 20 m s^{-1} or 40 knots, are responsible for *williwaws*. This wind speed image was derived from the NRCS image shown in Figure 13.4.

13.5 Validation and Future Developments

The full usefulness and potential of SAR wind imagery will be realized when it is possible to know with confidence that the surface roughness can be used to infer wind speed [Brown, 2001]. In order to validate wind speed retrievals, *Monaldo et al.* [2001] systematically compared RADARSAT-1 SAR wind speed measurements, initiated with model wind directions, with comparable National Data Buoy Center (NBDC) buoy wind speeds. For each buoy-SAR comparison, the SAR-derived wind speed was averaged over a 5-km radius circle around the buoy position. Buoy measurements are typically reported once per hour and averaged over 8 minutes. As a consequence, a buoy measurement could be reflecting local variability. The once-

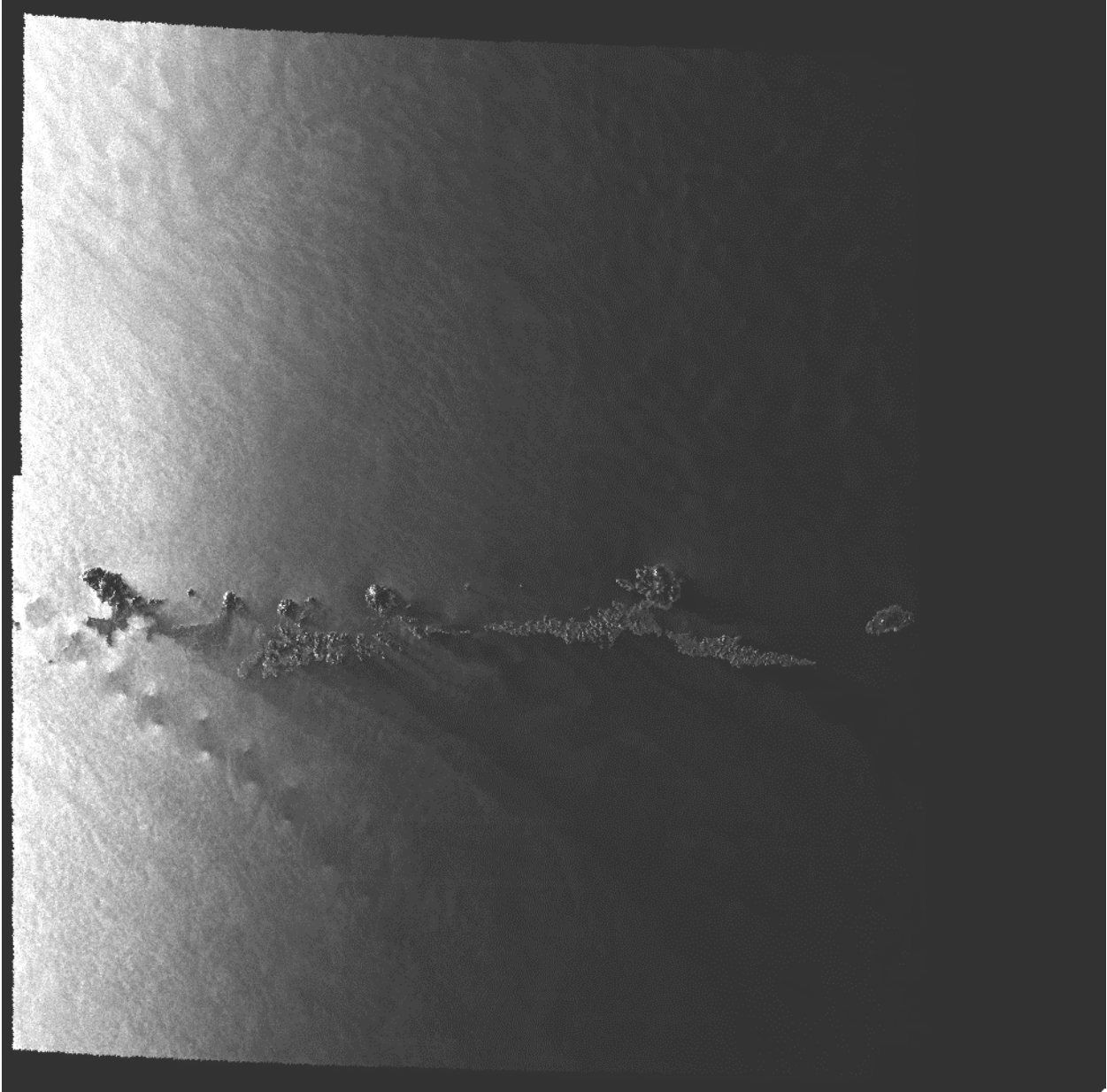


Figure 13.6. Vortex shedding from Gareloi Island in the Aleutian Islands. The radar cross section decreases with increasing nadir incidence from left to right. This image was acquired by RADARSAT-1 (C-band, HH) on 4 May 2001 at 0526 UTC. ©CSA 2001.

per-hour sampling guarantees that buoy and SAR comparisons are never separated by more than 30 minutes. The standard deviation between the SAR and buoy measured wind speed was 1.76 m s^{-1} , similar to comparisons achieved with conventional spaceborne scatterometers.

The natural extension of these buoy-SAR comparisons is the comparison between SAR and QuikSCAT scatterometer wind speeds. *Thompson et al.* [2001] compared these wind speeds for measurements made during the year 2000. Whenever a SAR overpass coincided with a QuikSCAT scatterometer measurement, the SAR wind speeds were averaged over an area of diameter of 25 km so that the two measurements would be comparable. The comparisons improved as the temporal difference between the two decreased. For time separations of less than 1 hour, the standard deviations were 2.3 m s^{-1} . At a separation of less than 15 minutes,

Wind Speed and Direction

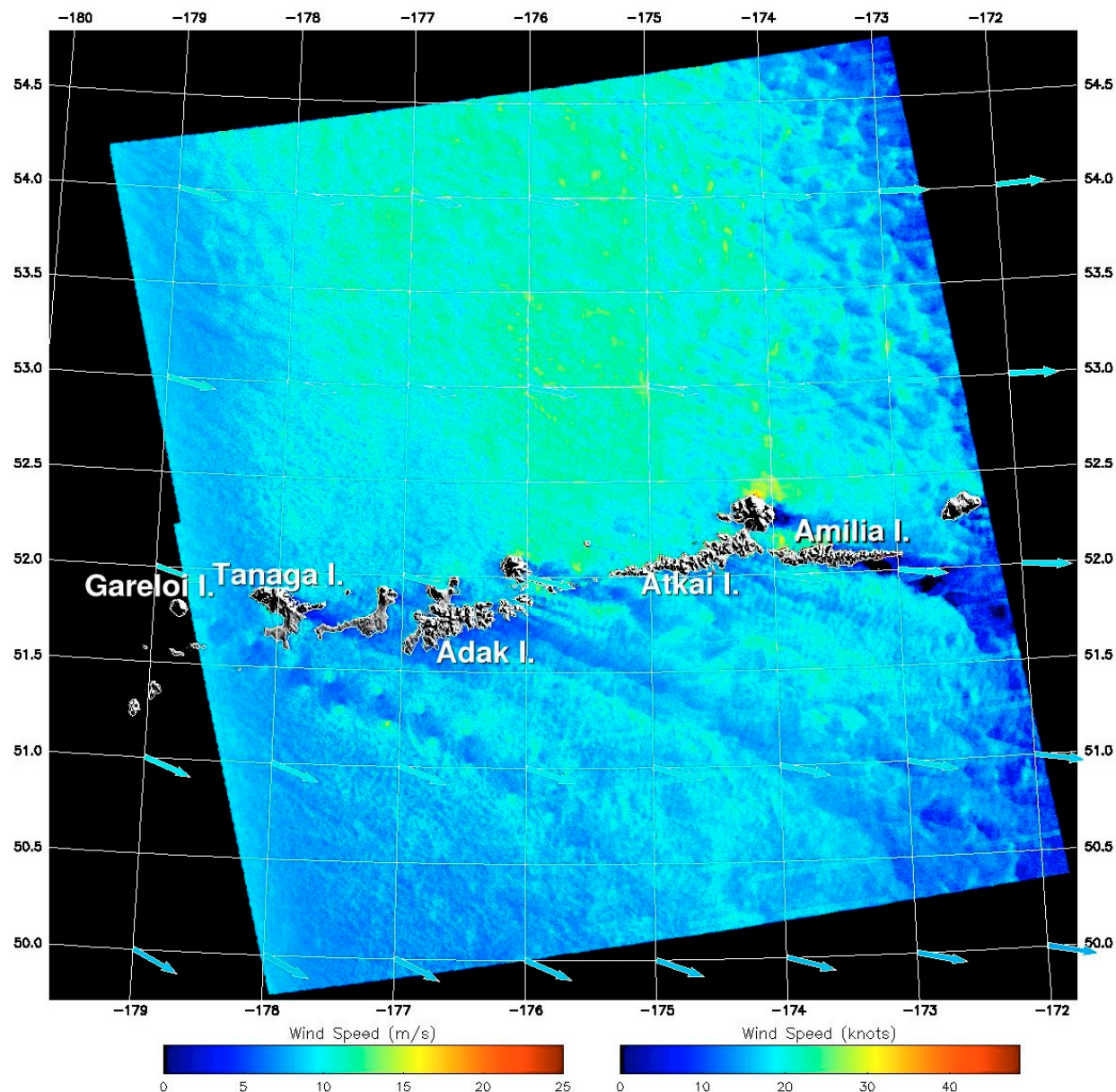


Figure 13.7. Vortex shedding from Gareloi Island in the Aleutian Islands. This wind speed image was derived from the NRCS image shown in Figure 13.6.

the standard deviation dropped to 2.0 m s^{-1} . The quality of the RADARSAT-1 SAR and QuikSCAT wind speed comparison is illustrated in Figure 13.10. The SAR data for Figure 13.10 were acquired on 31 January 2001 at 0335 UTC, the QuikSCAT data were acquired on the same day at 0438 UTC. The small colored arrows represent the QuikSCAT wind vector retrievals. The color codes for the SAR and scatterometer wind speeds in the figure are identical. As the smaller arrows disappear into the SAR wind speed fields, agreement increases. It is clear that the scatterometer picks up the increased wind speed for flow between Kodiak Island and the Kenai Peninsula. However, it misses the detailed structure apparent in the SAR wind speed field.

The key difficulty in SAR wind speed retrieval is determining the wind direction. The previous SAR-QuikSCAT comparisons were made using NOGAPS model wind predictions

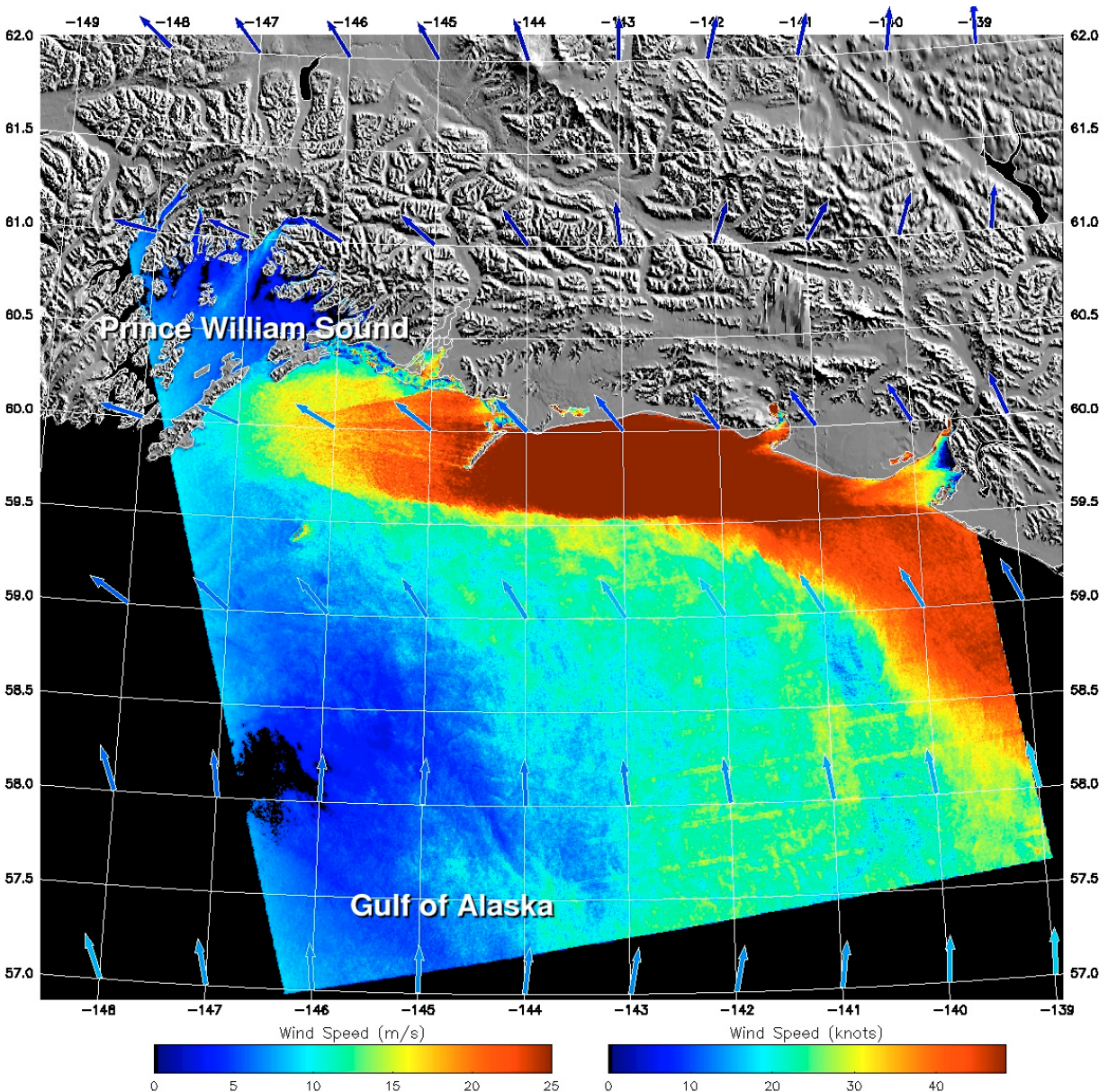


Figure 13.8. Wind speed image in northern part of the Gulf of Alaska. This wind flows to the north until it runs into topography along the coast forming a high-speed barrier jet along the coast. This image was derived from a RADARSAT-1 (C-band, HH) image acquired on 18 February 2000 0310 UTC .

interpolated down to the SAR pixel position to initiate the SAR wind retrieval. To quantitatively ascertain the effect of using the model directions for the retrieval, the retrievals were re-computed using the QuikSCAT wind directions. The use of these directions dramatically improves the SAR and QuikSCAT comparisons. When the temporal separation between measurements is 15 minutes or less, the standard deviation between wind speed measurements is as low as 1.34 m s^{-1} . This result suggests that if SAR and QuikSCAT data were routinely merged, (i.e., scatterometer wind directions were used, when available, for the SAR wind retrieval) the accuracy of SAR wind speeds would improve. The additional value of the SAR wind fields is that they extend to the shore and provide important information in coastal areas.

Wind Speed and Direction

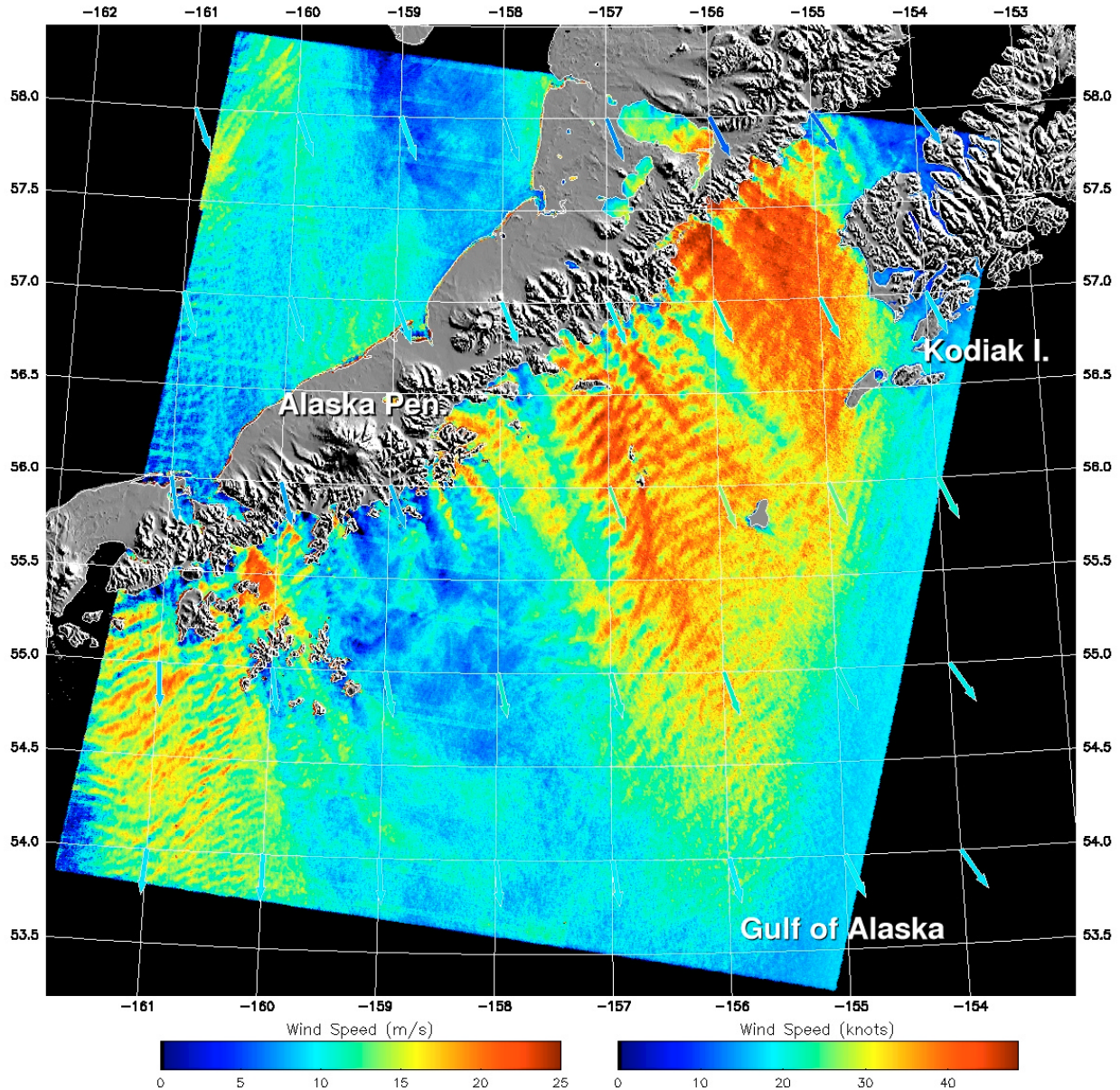


Figure 13.9. As the wind flows over the Alaska Peninsula atmospheric internal waves are generated. This image was derived from a RADARSAT-1 (C-band, HH) image acquired on 28 September 2000 1650 UTC.

13.6 Conclusion

Radar scatterometers like the ones on SEASAT, ERS-1, ERS-2, ADEOS-1, and QuikSCAT have matured to the point that they may be considered operational tools for global wind vector measurements. As important as these measurements are, the 25-km resolution of these instruments limits their applicability and usefulness in regions where higher resolution will reveal smaller scale phenomena, particularly in coastal areas. Recent research with high-resolution (sub-kilometer) SAR imagery shows promise for making wind speed measurements with better than 2 m s^{-1} accuracy. Moreover, by combining SAR NRCS measurements with scatterometer directions, wind speed measurements are further improved. The use of wind

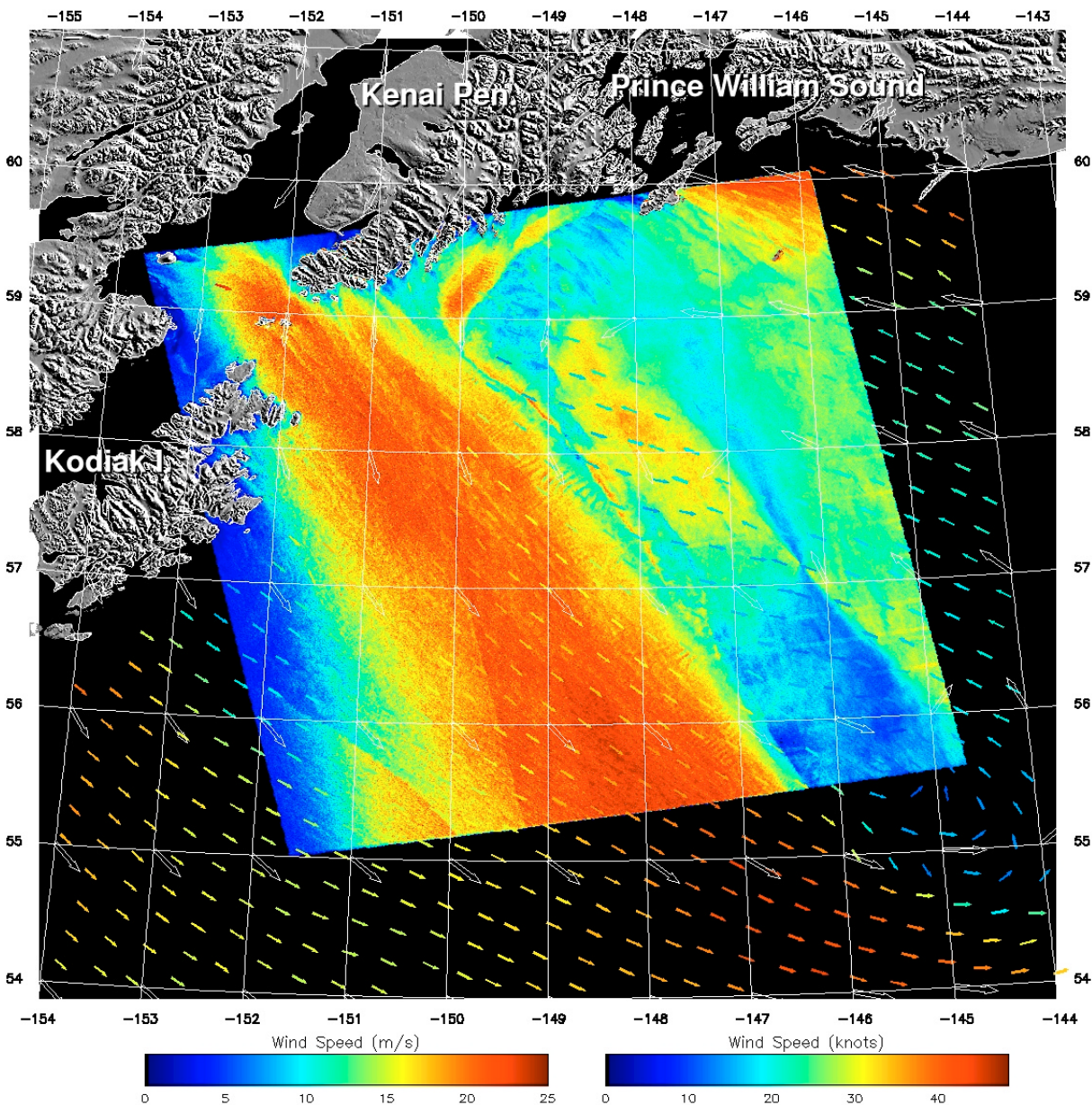


Figure 13.10. RADARSAT-1 (C-band, HH) SAR and QuikSCAT wind speed image. The small arrows are color-coded QuikSCAT wind speed retrievals. The SAR image was acquired on 31 Jan 2000 0335 UTC. The QuikSCAT data were acquired on the same day at 0438 UTC.

directions from the SAR imagery itself may also improve retrievals. The synergistic fusion of data from both instruments offers the greatest hope for wind field measurements in coastal areas from space.

13.7 References

- Alpers, W., U. Pahl, and G. Gross, 1998: Katabatic wind fields in coastal areas studied by ERS-1 synthetic aperture radar imagery and numerical modeling. *J. Geophys. Res.*, **103**, 7875–7886.
- Boggs, D. H., 1982: Seasat Scatterometer Geophysical Data Record (GDR) Users Handbook. Jet Propulsion Laboratory Document D-129, Pasadena, CA, 267 pp.

Wind Speed and Direction

- Bragg, W. L., 1913: The diffraction of short electromagnetic waves by a crystal. *Proc. Camb. Phil. Soc.*, **17**, 43–57.
- Brown, R. A., 1980: Longitudinal instabilities and secondary flows in the planetary boundary layer: A review. *Rev. Geophys.*, **18**, 683–697.
- , 1983: On satellite scatterometer capabilities in air–sea interactions. *J. Geophys. Res.*, **88**, 1663–1673.
- , 1986: On a satellite scatterometer as an anemometer. *J. Geophys. Res.*, **91**, 2221–2232.
- , 2001: On satellite model functions. *J. Geophys. Res.*, **105**, 29 195–29 205.
- , and F. Lee, 1972: A shooting method application to the stability problem for stratified rotation boundary layers. *J. Comput. Phys.*, **10**, 107–122.
- Fetterer, F., C. C. Wackerman, and D. Gineris, 1998: Validating a scatterometer wind algorithm for ERS-1 SAR. *IEEE Trans. Geosci. Remote Sens.*, **36**, 479–492.
- Fu, L. L., and B. Holt, 1982: Seasat views oceans and seas with synthetic aperture radar. Jet Propulsion Laboratory Publ. 81–102, Pasadena, CA, 200 pp.
- Gerling, T. W., 1986: Structure of the surface wind field from the Seasat SAR. *J. Geophys. Res.*, **91**, 2308–2320.
- IFREMER, Off-line Wind Scatterometer ERS Products - User Manual: Version 2.0, C2-MUT-W-0101F, March 1996.
- Hawkins, J. D., and P. G. Black, 1983: Seasat scatterometer detection of gale force winds near tropical cyclones. *J. Geophys. Res.*, **88**, 1674–1682.
- Horstmann, J., W. Koch, S. Lehner, and R. Tonboe, 2000: Wind retrieval over the ocean using synthetic aperture radar with C-band HH polarization. *IEEE Trans. Antennas Propag.*, **14**, 749–754.
- Jones, W. L., V. E. Delnore, and E. M. Bracalente, 1981: The study of mesoscale ocean winds. *Spaceborne Synthetic Aperture Radar for Oceanography*, R. C. Beal, P. S. DeLeonibus, and I. Katz, Eds., The Johns Hopkins University Press, 87–94.
- Pichel W. G., and P. Clemente-Colón, 2000: NOAA CoastWatch SAR applications and demonstration. *Johns Hopkins APL Tech. Dig.*, **21**, 49–57.
- Pierson, W. J., 1983: The measurement of the synoptic scale wind over the ocean. *J. Geophys. Res.*, **88**, 1683–1708.
- Monaldo, F. M., D. R. Thompson, R. C. Beal, W. G. Pichel, and P. Clemente-Colón, 2001: Comparison of SAR-derived wind speed and model predictions and ocean buoy measurements. *IEEE Trans. Geosci. Remote Sens.*, **39**, 2587–2600.
- Overland, J. E., 1984: Scale analysis of marine winds in straits and along mountainous coasts. *Mon. Wea. Rev.*, **112**, 2530–2534.
- Moore, R. K., and Coauthors, 1974: Simultaneous active and passive microwave response of the Earth—The Skylab RADSCAT experiment. *Proc. Ninth Int. Symp. on Remote Sensing of the Environment*, Ann Arbor, MI, Environmental Research Institute of Michigan, 189–217.
- Romeiser, R., W. Alpers, and V. Wisman, 1997: An improved composite surface model for the radar backscattering cross section of the ocean surface, 1, Theory of the model and optimization/validation by scatterometer data. *J. Geophys. Res.*, **102**, 25 237–25 250.
- Spencer, M. W., C. Wu, and D. G. Long, 2000: Improve resolution backscatter measurements with the SeaWinds pencil-beam scatterometer. *IEEE Trans. Geosci. Remote Sens.*, **38**, 89–104.
- Stofflen, A., and D. Anderson, 1997: Scatterometer data interpretation: Measurement and inversion. *J. Atmos. Oceanic Technol.*, **14**, 1298–1313.

- Thompson, D. R., T. M. Elfouhaily, and B. Chapron, 1998: Polarization ratio for microwave backscattering from the ocean surface at low to moderate incidence angles. *Proc. 1998 Int. Geoscience and Remote Sensing Symp.*, Seattle WA, IEEE, 1671–1673.
- , F. M. Monaldo, R. C. Beal, W. G. Pichel, and P. Clemente-Colón, 2001: The use of RADARSAT SAR imagery with QuikSCAT wind directions for high-resolution coastal wind mapping. *Eos, Trans. Amer. Geophys. Union*, **82**, 469–474.
- Vachon, P. W. and F. W. Dobson, 1996: Validation of wind vector retrieval from ERS-1 SAR images over the ocean, *The Global Atmos. and Ocean*, **4**, 177-187.
- Wackerman, C. C., C. L. Rufenach, R. A. Shuchman, J. A. Johannessen, and K. L. Davidson, 1996: Wind vector retrieval using ERS-1 synthetic aperture radar imagery, *IEEE Trans. Geosci. Remote Sens.*, **34**, 1343-1352.
- Weissman, D. E., D. King, and T. W. Thompson, 1979: Relationship between hurricanes surface winds and L-band radar backscatter from the sea surface. *J. Appl. Meteor.*, **18**, 1023–1034.
- Wentz, F. J., S. Peteherych, and L. A. Thomas, 1984: A model function for ocean radar cross sections at 14.6 GHz. *J. Geophys. Res.*, **89**, 3689–3704.
- , L. A. Mattox, and S. Peteherych, 1986: New algorithms for microwave measurements of ocean winds: Applications to Seasat and the Special Sensor Microwave Imager. *J. Geophys. Res.*, **91**, 2289–2307.
- Wright, J. W., 1960: Backscattering from capillary waves with application to sea clutter. *IEEE Trans. Antennas Propag.*, **14**, 749–754.